Calculation of the electronic structure and the magnetic properties of $SrRuO_3$ and $CaRuO_3$

1997 J. Phys.: Condens. Matter 9 9563

(http://iopscience.iop.org/0953-8984/9/44/012)

J. Phys.: Condens. Matter **9** (1997) 9563–9584. Printed in the UK PII: S0953-8984(97)82624-0

Calculation of the electronic structure and the magnetic properties of $SrRuO_3$ and $CaRuO_3$

G Santi and T Jarlborg

Département de Physique de la Matière Condensée, Université de Genève, CH-1211 Genève 4, Switzerland

Received 14 March 1997, in final form 11 August 1997

Abstract. We study the two pseudo-cubic perovskite ruthenates $SrRuO_3$ and $CaRuO_3$, by means of LSDA electronic structure calculations using the LMTO method for both the idealized cubic and the real orthorhombic structures. The LSDA calculations predict that both orthorhombic structures are ferromagnetic, with magnetic moments of 2.0 and 1.9 μ_B respectively, while in the cubic structure, only $SrRuO_3$ is magnetic (1.7 μ_B). The general features of the DoS are in reasonable agreement with the experimental photoemission and EELS spectra. However, the fine details of the DoS of these structures are sharply peaked near the position of ϵ_F and this contributes to the high sensitivity of many of the calculated results as well as to strong variations of the properties of the real material. Magnetic moments and transport properties are examples of quantities exhibiting strong variations, but the calculations clearly show that the orthorhombic distortion is favourable for large spin splitting and low conductivity. A gap structure in the majority band just above ϵ_F can be important for semi-metallic properties induced by distortions or charge transfers.

1. Introduction

Although ternary oxides have been known about for a long time [1], it is only recently, since the discovery of the superconducting oxides, that they have been studied intensively. Among them, $SrRuO_3$ (SRO) and $CaRuO_3$ (CRO) are particularly interesting, since SRO is one of the rare ferromagnetic 4d materials, while CRO appears to be non-magnetic. They are chemically close to a number of very interesting compounds such as the non-cuprate superconducting oxide Sr_2RuO_4 [2, 3] or the second member of the $(SrO)_{n+1}(RuO_2)_n$ series, $Sr_3Ru_2O_7$, that was found to develop strong antiferromagnetic correlations below 15 K [4]. The difference between the magnetic properties of SRO and the other ruthenates is striking, since none of the latter compounds are found to be ferromagnetic. For instance, another ruthenate, $BaRuO_3$, that has recently been investigated via photoemission [5], is also non-magnetic (but has another arrangement of the RuO_6 octahedra).

There is much technical interest in using perovskite oxides for ferroelectric and superconducting applications [6], and SRO has been investigated as an electrode material for these applications because of its metallic character and close lattice match with several ferroelectric oxides (e.g. in ferroelectric transistors [7]) and the high-temperature superconductors. Easy growth and good stability of epitaxial thin films are obtained [8, 9], and their properties resemble those of good single crystals [10]. This, together with the small lattice mismatch with $YBa_2Cu_3O_{7-\delta}$ (YBCO), makes SRO and CRO very good candidates for the fabrication of superconducting multilayers [11–14]. In this case, the magnetic

0953-8984/97/449563+22$19.50

properties of SRO have been used to show the decoupling of the vortices thst would occur if the thickness of SRO were larger than 50 Å [14]. SRO has also been used in the fabrication of ferroelectric heterostructures with $Pb(Zr_{0.52}Ti_{0.48})O_3$ (PZT) [15]. Recently, a ferroelectric field effect has been demonstrated using PZT in ultrathin SRO films, in which a non-volatile, reversible resistivity change of 10% was measured [16, 17].

SRO, CRO and $Sr_{1-x}Ca_xRuO_3$ all have an orthorhombic structure which is a distorted perovskite structure [18–20]. SRO, whose distortion is small, was found to become cubic above about 800 K whereas CRO remained orthorhombic up to ≈1700 K [21, 22]. It is a weak ferromagnet with $T_C \approx 160$ K and $\mu_{\rm sat}$ in the range 0.85–1.6 μ_B [23–28]. Callaghan *et al* proposed a model relying on the 2/3 occupancy of the lower-lying t_{2g} Ru d band [24] which implies $S = 1$ spin magnetism in good agreement with the measured effective magnetization $\mu_{\rm eff} = 2.4\ \mu_B$ [26]. This compound also shows a large magnetocrystalline anisotropy with one easy axis (*a* or *b*) [23, 26] which is reflected in the anisotropy of the remnant magnetization observed in thin films [29]. Three reasons for the reduced magnetic moment $\mu_{\rm sat}$ have been given, i.e. spin canting [24], collective-electron (band) magnetism [25], and the multidomain structure observed by Kanbayashi combined with the large magnetocrystalline anisotropy [30]. It has also been found that the Curie temperature, T_C, decreases with increasing pressure [20, 31] and with increased Ca doping [20]. Furthermore, Kiyama *et al* recently reported the observation of an Invar effect that suggests strong similarities between SRO and 3d Invar alloys [32]. In addition, SRO exhibits an anomalous Hall effect [23, 33, 34], and magnetoresistance measurements show that two competing mechanisms are at work in the low-field (positive magnetoresistance) and the high-field regions (negative magnetoresistance) [35].

CRO, on the other hand, which was first thought to be antiferromagnetic [25], does not show any long-range order [36, 37]. This striking asymmetry between the magnetic properties of these two very close systems was tentatively explained by the correlation between the orthorhombic distortion and the onset of antiferromagnetic interaction [38, 39], or by the special role played by the Sr^{2+} cation [38] (providing a kind of spin-transfer bypass between O atoms). We shall propose here an alternative explanation based on the high and peaked density of states (DoS) at ϵ_F and the change in the size of the cell. Fukunaga and Tsuda proposed that there was some spin-scattering mechanism preventing CRO from becoming antiferromagnetic [39]. This idea seems to be supported by the recent result showing that CRO doped with Na is antiferromagnetic [40].

SRO and CRO have some other unusual properties that are presumably connected to the difference in their magnetism. They are both metallic, and the resistivity $\rho(T)$ shows the expected kink at T_C for SRO [10, 33, 27, 28, 41] but nothing similar for CRO [10]. Klein *et al* recently claimed that an unusual interplay between the transport and the magnetic properties of SRO could explain the strong divergence of $\mathrm{d}\rho/\mathrm{d}T|_{T=T_C^+}$ [27, 28]. An anomaly in the optical phonon spectrum near T_C was attributed by Kirillov *et al* to a lattice distortion induced by the magnetic ordering [42]. The large measured electronic specific heat in SRO [33, 43] indicates that electron–phonon coupling or even spin fluctuations are important. Moreover, the specific heat was compatible with an unusual T^2-law for the magnetization [44], which is another indication of the peculiar properties of this material.

Despite such a large experimental interest in these systems, they have not attracted many *ab initio* theoretical studies. Except for a review of the electronic structures of many perovskite ABO_3 ternary oxides [45] that does not include the SRO nor CRO compounds, and our calculation [33] that we present in detail here, we know only of the calculation of Singh for SRO [46]. As we shall see, we mainly reach the same conclusions as Singh for $SrRuO_3$.

The organization of this paper is as follows. In section 2 we briefly describe the structural parameters and the method of calculation. The results for the electronic structure, the transport and the magnetic properties are presented in section 3. In section 4, we compare our results with the observed photoemission and EELS spectra, discuss the sensitivity of the calculations and the magnetic properties, and present a simple application of our results to the case of a thin layer of SRO grown on a ferroelectric. Finally, section 5 contains a summary and conclusions.

2. Details of the calculation

The symmetry of SRO and CRO is orthorhombic, of the $GdFeO_3$ type, having a space group *Pnma*, with 4 f.u. per cell. As we already mentioned, they can be considered as distorted simple cubic perovskites. We used the lattice parameters from the experiment, i.e. for SRO, $a = 5.53$ Å, $b = 5.57$ Å, $c = 7.85$ Å [20], and for CRO, whose distortion is larger, $a = 5.36$ Å, $b = 5.52$ Å, $c = 7.66$ Å [19]. We also considered the idealized simple cubic case with $a = b = c = 3.92$ Å and 3.84 Å for SRO and CRO respectively.

The calculations were performed using the LMTO method [47, 48] within the LSDA [49], with s, p and d basis functions for all atoms. Relativistic terms are included except for the spin–orbit coupling of the valence bands. Core states are relaxed during the self-consistency process. We used a mesh of 120 k-points in the irreducible Brillouin zone (IBZ) for the simple cubic calculation, 64 for SRO in the orthorhombic structure, and 216 for orthorhombic CRO. In addition, for each case we performed both magnetic (i.e. spin-polarized) and non-magnetic calculations. The energy range of the valence bands is large due to high 'semi-core' states such as O s, Sr p and Ca p. This represents a difficulty for linearized methods, since the bands within such a wide energy window have to be described well from one linearization energy. The Sr 4p electrons were included in the valence, since the energy of the 4p core level is close to the O 2s valence level. In CRO, the Ca 3p core level is lower, and therefore it does not need to be included in the valence. Nevertheless, for the sake of comparability with SRO, we included this level in the valence. This is not a serious problem since the Ca 4p and Sr 5p levels are expected to lie far above ϵ_F. In our earlier calculation, the linearization energy was chosen further away from ϵ_F and some bands far above ϵ_F became too wide and affected the bands from ϵ_F and above [33]. Now we linearize closer to ϵ_F in order to have a good description of the Fermi surface (FS). For SRO we obtain similar band features to those in the work of Singh [46].

Since ϵ_F falls near a sharp peak of the DoS, it turns out that small changes in certain calculational parameters (like the linearization energy) that usually do not affect the results can have large effects in these systems. The choice of the Wigner–Seitz (WS) radii r_{WS} is such a detail which may be critical due to the sensitivity at the FS. Here they were set by minimizing the interstitial volume between the muffin-tin spheres. For SRO, we used radii of 1.85 Å for Sr, 1.43 Å for Ru and 1.20 Å for O. For CRO, we scaled these radii with the lattice constant. This leads to 1.81 Å for Ca, 1.40 Å for Ru and 1.17 Å for O. However, test calculations with different choices did not reveal a strong sensitivity.

We also performed calculations on SRO with a tetragonal distortion to simulate the effect of the (small) lattice mismatch with $SrTiO_3$, the typical substrate for the thin films, on the first few layers of SRO. In the case of the orthorhombic SRO, we also tried the structure found by Kobayashi *et al* [19] which is slightly different from the one that we used here to check the sensitivity of the calculated properties to some change in the parameters. We compare the results of these calculations with our main ones in sections 3 and 4.

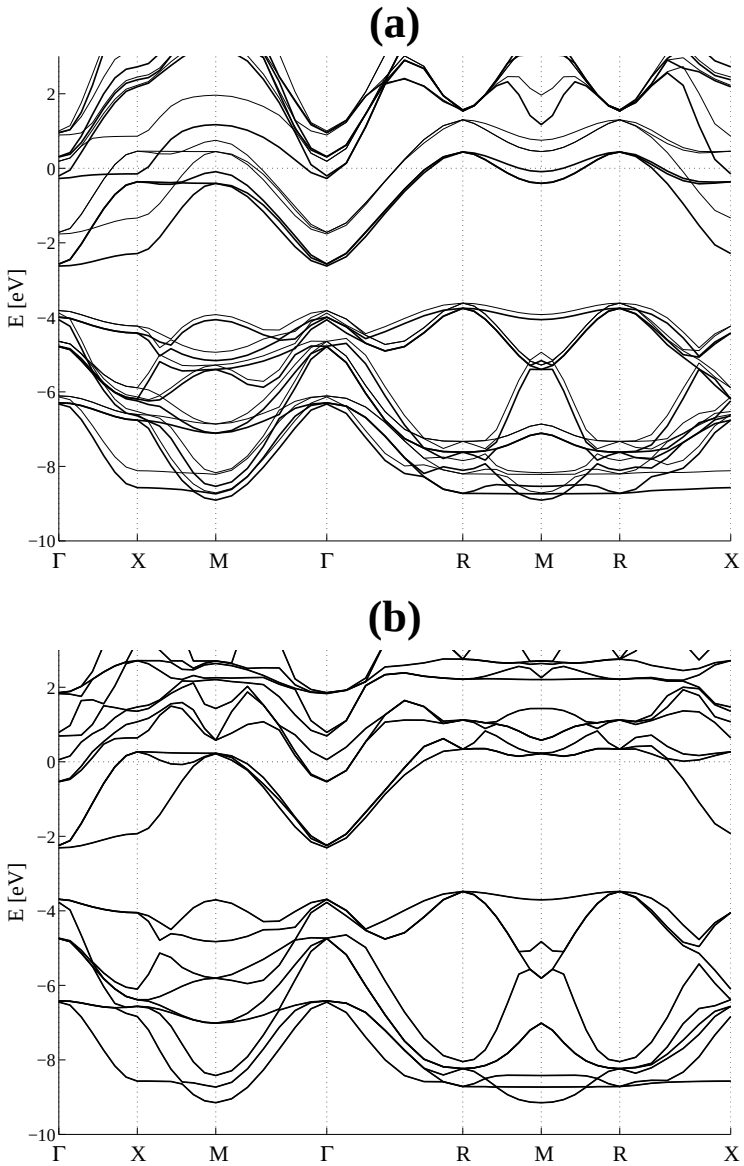

Figure 1. The band structure for magnetic (a) $SrRuO_3$ and (b) $CaRuO_3$ in the idealized simple cubic perovskite structure. The thin lines correspond to minority-spin bands. Note that there is no spin splitting for CRO. (ϵ_F is set to 0.)

3. Results

3.1. Electronic structure

The band structures of idealized simple cubic magnetic SRO and CRO are shown in figure 1. The cubic band structure can be split basically into three regions (see also the DoS in figures 2 and 3): they are mainly of Sr or Ca d character above ϵ_F, Ru d character around ϵ_F, and O p character below the gap. For SRO, the spin splitting at Γ is 0.46 and 0.18 eV

Table 1. The partial and total DoS at ϵ_F for $SrRuO_3$ in states eV^{-1} $cell^{-1}$ $spin^{-1}$ (except for the results of non-polarized calculations and the sums of the two spin channels which are in states eV^{-1} $cell^{-1}$ $spin^{-1}$). We present here the DoS per atom, as well as the percentage of the dominant p or d character for each atom. Note that there are four formula units (f.u.) in the orthorhombic cell. (The DoS for an atom is the sum of the DoS of all atoms of this type.)

		Sr		Ru		O_3		
(eV^{-1} $cell^{-1}$ $spin^{-1}$)		Total	(% of Sr d)	Total	(% of Ru d)	Total	(% of O p)	$N(\epsilon_F)$
Orthorhombic								
Magnetic	(↑)	0.06	(67)	1.49	(99)	0.44	(86)	1.99
	(↓)	0.23	(91)	4.76	(99)	1.29	(72)	6.28
	(↑↓)	0.29	(90)	6.24	(100)	1.73	(75)	8.27
Non-magnetic		0.58	(88)	13.17	(99)	3.70	(77)	17.44
Cubic								
Magnetic	(↑)	0.05	(89)	0.83	(100)	0.22	(69)	1.10
	(↓)	0.07	(92)	1.04	(100)	0.27	(69)	1.37
	(↑↓)	0.11	(91)	1.87	(100)	0.49	(69)	2.47
Non-magnetic		0.29	(87)	6.59	(100)	1.85	(82)	8.73

Table 2. The partial and total DoS at ϵ_F for $CaRuO_3$ in states eV^{-1} $cell^{-1}$ $spin^{-1}$. The same remarks apply as for table 1. No spin splitting was found in cubic CRO, and the solutions of the magnetic and non-magnetic calculations are identical.

		Ca		Ru		O_3		
(eV^{-1} $cell^{-1}$ $spin^{-1}$)		Total	(% of Ca d)	Total	(% of Ru d)	Total	(% of O p)	$N(\epsilon_F)$
Orthorhombic								
Magnetic	(↑)	0.08	(75)	1.07	(100)	0.26	(88)	1.41
	(↓)	0.65	(92)	7.02	(99)	1.77	(66)	9.43
	(↑↓)	0.73	(89)	8.09	(99)	2.03	(69)	10.84
Non-magnetic		0.67	(64)	16.24	(99)	3.95	(73)	20.86
Cubic								
Non-magnetic		1.12	(92)	4.12	(100)	1.26	(71)	6.50

in the Ru d and O p regions, respectively. The corresponding calculation for cubic CRO gives a non-magnetic solution. In contrast, the real-structure calculations give ferromagnetic solutions for both SRO and CRO with spin splittings near ϵ_F of about 1 and 0.2 eV in the Ru d and O p regions, respectively.

We present the DoS and the most important partial DoS (PDoS) in figure 2 for the cubic case and in figure 3 for the orthorhombic one. These figures show clearly the different regions that we have just described as well as the importance of the hybridization. We also present the DoS and PDoS at ϵ_F in tables 1 and 2 for majority spins (↑) and minority spins (↓).

The figures displaying the DoS show that ϵ_F falls on the side or near the top of a large

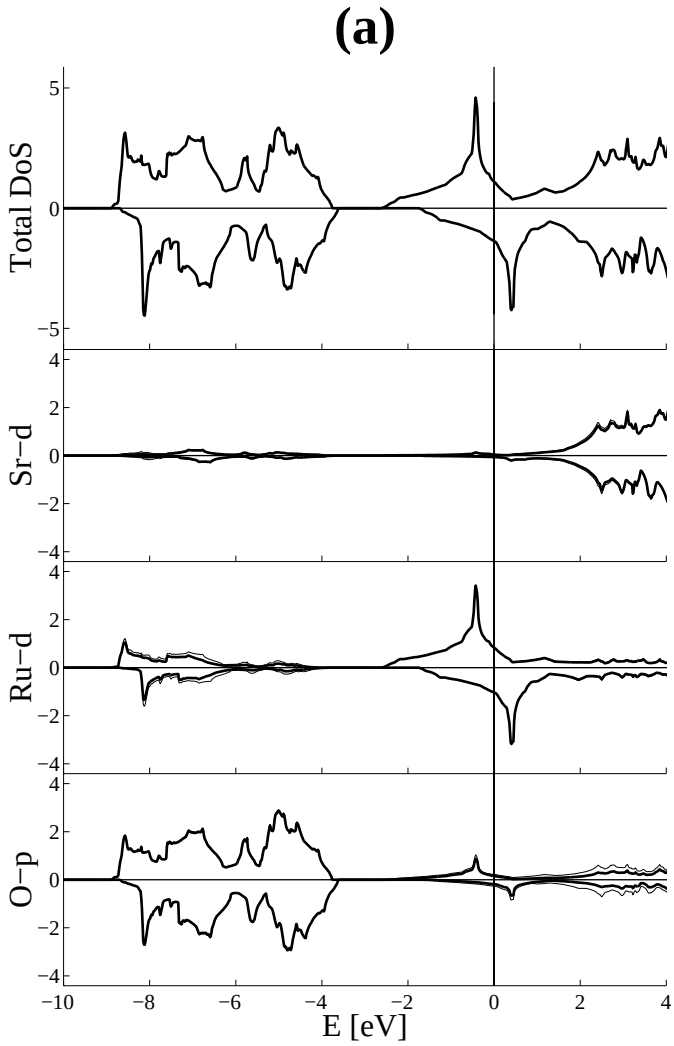

Figure 2. The total and partial DoS in states eV^{-1}/(f.u. spin) for (a) SRO and (b) CRO in the idealized cubic structure for the spin-polarized calculation (the energies are in eV). The majority-spin electrons' DoS is positive and the minority one is negative. We show the d DoS for Sr, Ca, Ru, and the p DoS for O. In the partial DoS panels, the thin line (which is often difficult to distinguish from the thick one) denotes the total DoS for this atom.

DoS peak in these systems. Small modifications in the calculations, or in the real system (shear, charge transfer or doping), can make ϵ_F climb or descend on that peak. Since the condition for magnetism is sensitive to the DoS value at ϵ_F, such a small modification may or may not trigger ferromagnetic ordering. This fact provides a possible explanation of why a normally unimportant exchange of Sr with Ca will make magnetism disappear in the Ru 4d band. This delicate situation also illustrates why some calculated results are difficult to obtain very precisely. A high DoS peak in the cubic structures will be split by some distortion and lead to greater stability as in the real orthorhombic structures. A comparison of the total energies between the magnetic and non-magnetic configurations can be made, but comparisons between the cubic and distorted structures are more difficult since our

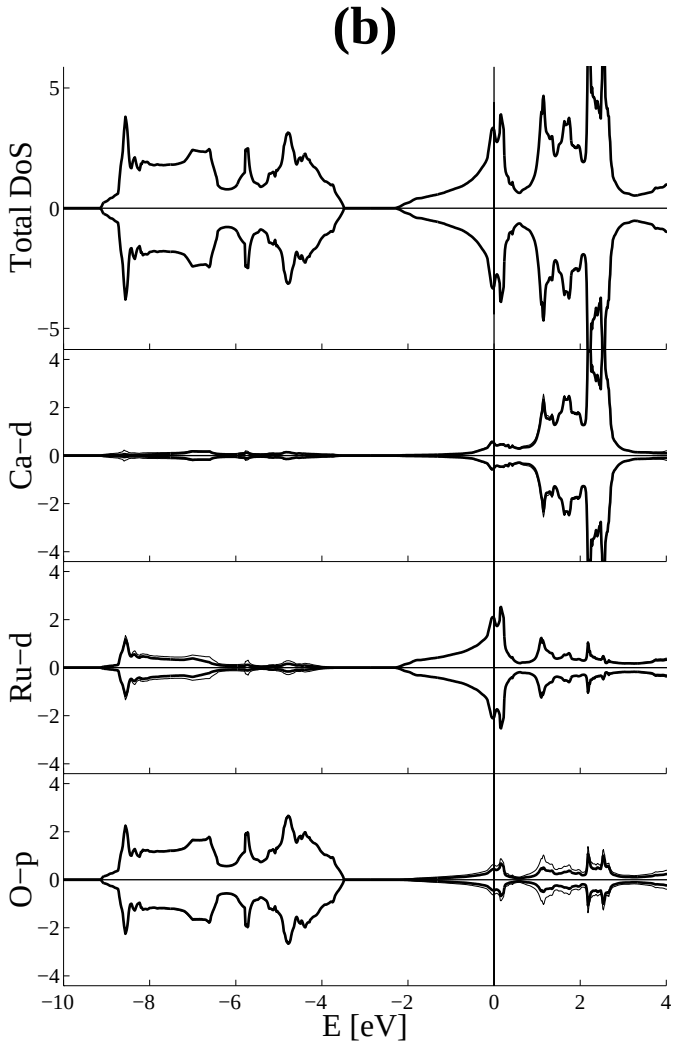

Figure 2. (Continued)

calculations use spherical potentials.

Between the Ru d and the O p regions, we find a gap of 1.2 eV for cubic SRO and 1.4 eV for CRO (1.1 eV and 1.3 eV in the orthorhombic case). This is consistent with the results of Takegahara for similar oxides [45], but disagrees with the results of Singh [46] who does not find any gap in his cubic electronic structure.

In a cubic crystal field, the Ru d bands split into a t_{2g} triplet and an e_g doublet. In the case of SRO, at Γ these bands are at -2.6 eV for t_{2g} and -0.2 eV for e_g. The e_g bands hybridize rather strongly with Sr d and O d. The large peak in the DoS seems to be due mainly to three flat bands: a d_{e_g} band between Γ and X and two $d_{t_{2g}}$ bands between X and M. In the case of SRO, the flat parts of these bands lie at almost the same energy, whereas in the CRO case, they are moved away from each other and give two peaks (see the total DoS panel for CRO in figure 2(b)) therefore reducing the DoS at ϵ_F and the propensity for magnetism. For the orthorhombic case, the peak splits into many subpeaks due to the

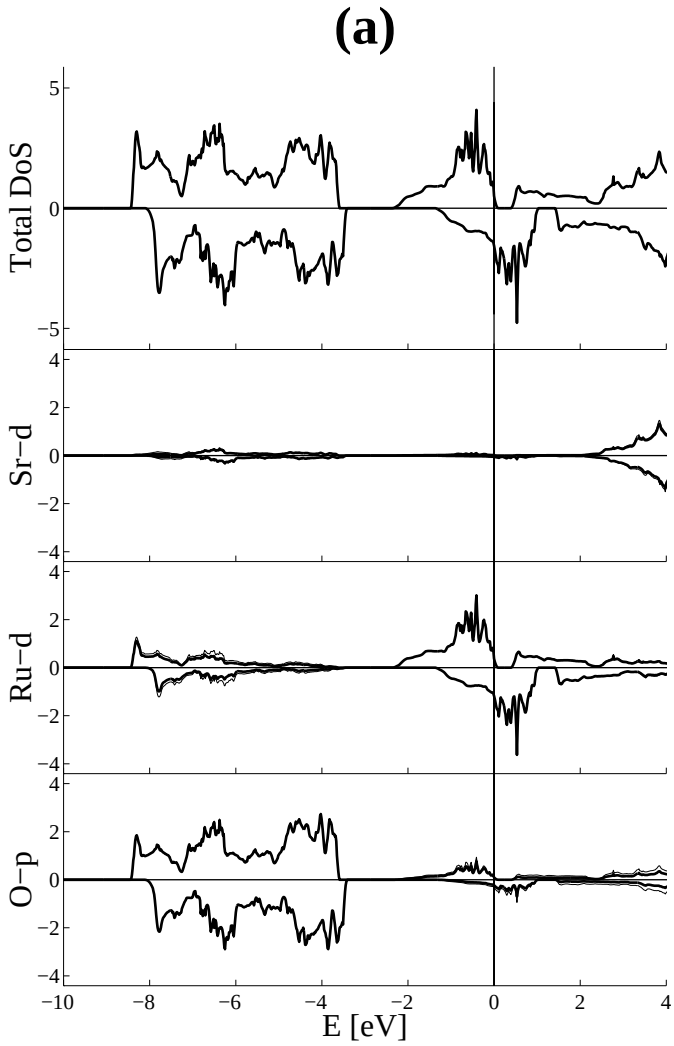

Figure 3. Total and partial DoS in states eV^{-1}/(f.u. spin) for (a) SRO and (b) CRO in the real orthorhombic structure (energies in (eV)). We show the same partial DoS as in figure 2.

symmetry breaking, but the substitution of Ca tends to broaden these peaks (see figure 3), consistently with the cubic result (for instance, in figure 3(b), there is a strong depression in the DoS for orthorhombic CRO near ϵ_F, at approximately -0.8 eV in the majority-spin DoS, that could be the signature of the splitting of the peak seen in figure 2(b) for cubic CRO).

In the orthorhombic case, figure 3 clearly shows the opening of a 'semi-gap' above ϵ_F that is completely absent of the cubic case. This semi-gap of about 0.30 eV for SRO and 0.50 eV for CRO is quite close to ϵ_F. This feature becomes interesting in the case of charge transfer or increased exchange splitting, when the majority band becomes completely filled to form a half-metallic ferromagnet. The gap is also present in the non-magnetic calculations.

In order to illustrate the bands further, we show the different sheets of the Fermi surface for the cubic SRO in figure 4. For majority-spin electrons, the three t_{2g} bands form three

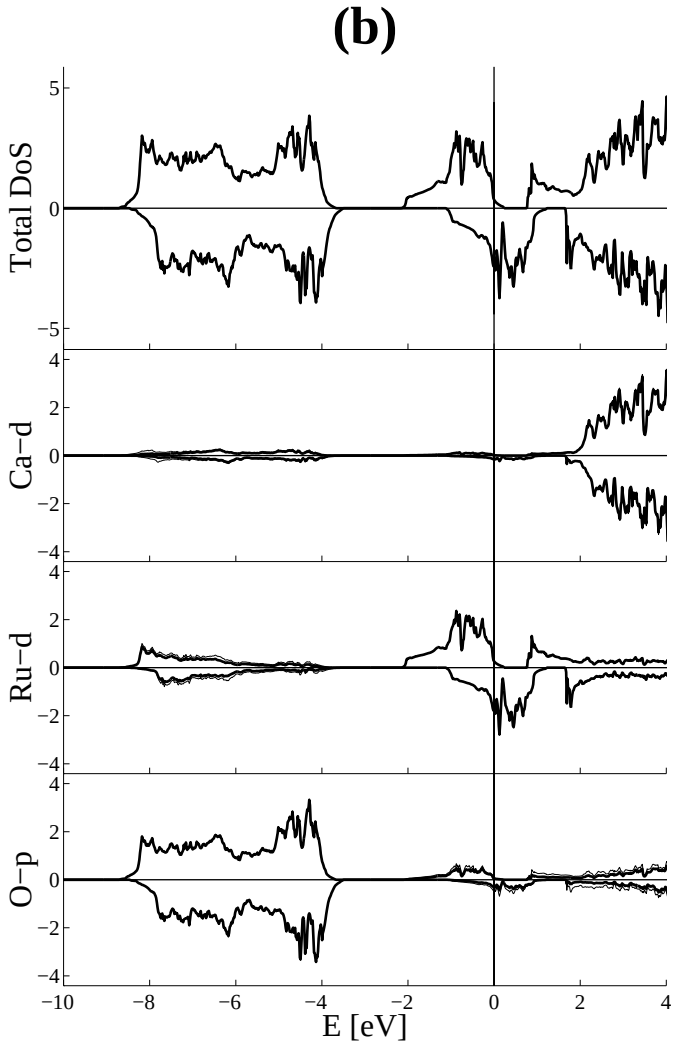

Figure 3. (Continued)

hole pockets centred on R, and the two e_g bands form one electron pocket and one electron-like 'jungle-gym' centred on Γ. For the minority electrons, only the t_{2g} bands cross ϵ_F giving rise to two electron spheres and one electron-like 'fat jungle-gym' around Γ.

Finally, figure 5 shows the spin-polarized FS for the real structure of SRO, as well as the bands in the vicinity of the Fermi level. The different sheets are plotted from a single-iteration calculation with 1331 *k*-points in the irreducible wedge. The band structure shows that bands crossings are likely to occur near the Fermi energy, explaining the odd shape of the sheet originating from the lower majority-spin band crossing ϵ_F (see figures 5(a) and 5(g)). This sheet will be very sensitive to small shifts of ϵ_F due to its very small dispersion in some parts of the BZ. A paramagnetic band structure has a much more stable FS than a spin-polarized one as in the present case, since the band splitting (and therefore the position of ϵ_F relative to bands' features) easily changes with the magnetic moment, while the parmagnetic FS is determined by the number of electrons. To verify the stability of the

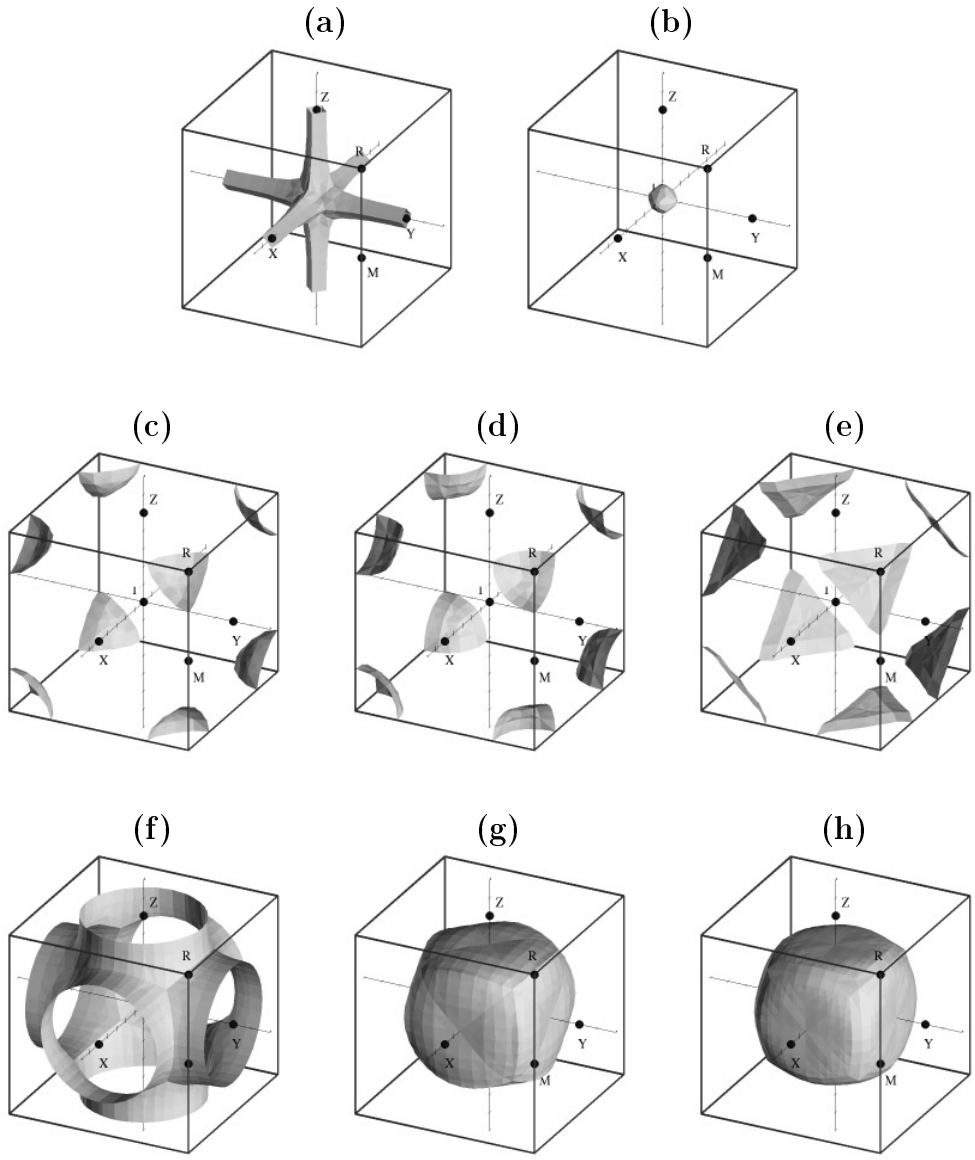

Figure 4. The different sheets of the Fermi surface of cubic SRO in the BZ. There are five bands crossing ϵ_F for the majority-spin electrons, (a)–(e). The first two, (a) and (b), that are centred on Γ are due to the e_g bands, and the three others, (c)–(e), centred on R are due t_{2g} bands. The three sheets for the minority-spin electrons, (f)–(h), are all due to t_{2g} bands. Note that the (c) and (d) sheets (majority electrons), as well as the (g) and (h) ones (minority electrons) are almost degenerate.

FS, we have examined different rigid-band shifts. The topology of the minority-spin sheets (figures 5(c)–5(f)) is essentially unchanged by rigid-band shifts (mainly, the sheets seem to move away from Γ when the minority-spin bands are shifted downwards and to shrink when they are shifted upwards). The sheet shown in figure 5(a) vanishes for a downwards shift of the majority-spin bands of about 40 meV. Furthermore, a shift of about 70 meV

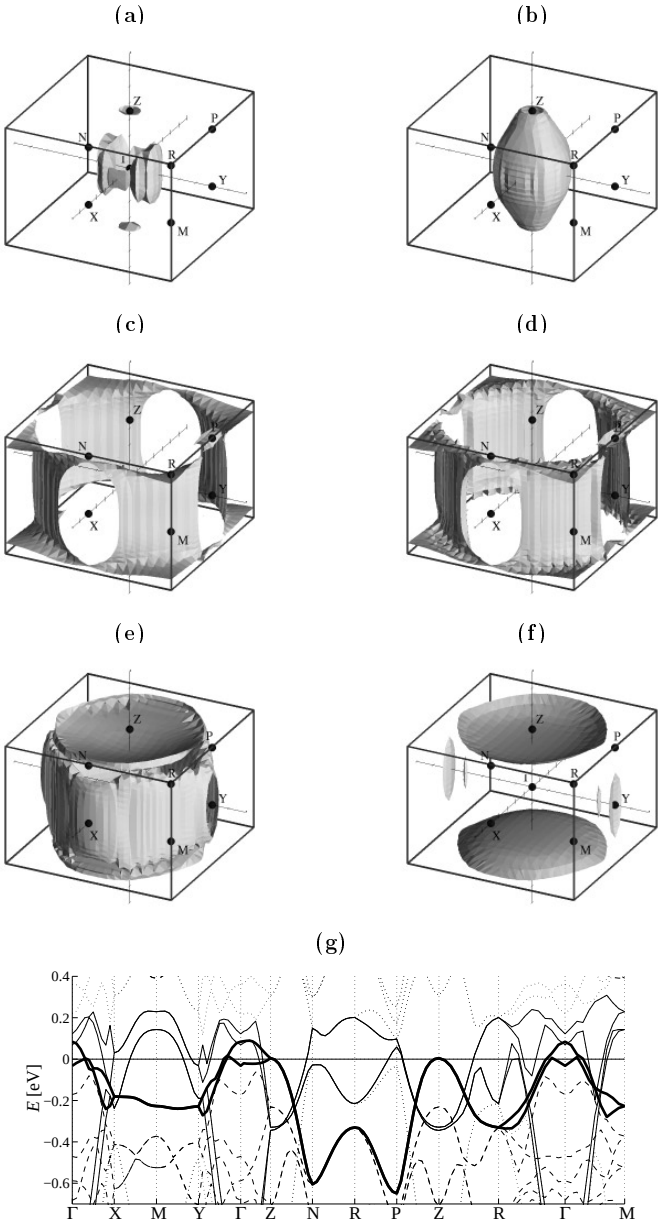

Figure 5. The different sheets of the Fermi surface of orthorhombic SRO (real structure) in the BZ. (a), (b) The two sheets from the majority-spin electron (↑) bands. (c)–(f) The four minority-spin electron (↓) sheets. The sheets of the FS were reconstructed from a calculation with 1331 k-points in the irreducible wedge. The sheets within each spin are sorted according to the energy of the bands that they originate from (from low- to high-energy bands). (g) The band structure in the vicinity of ϵ_F for orthorhombic spin-polarized SRO. We represent the two ↑ bands crossing ϵ_F (plain thick lines), the four ↓ ones (plain medium lines), as well as the other bands, with thin lines (dashed for ↑ and pointed for ↓). Note that it sometimes occurs that a small part of a sheet is attributed to another one due to band crossings (as in (f), for instance, with the small piece between Γ and Y).

Table 3. Transport properties for $SrRuO_3$ at $T = 0$. The DoS at ϵ_F can be obtained from table 1. The tensor $(n/m)_{\alpha\beta}$ is calculated from equation (2). The mean free path ℓ and the relaxation time τ have been calculated from the experimental resistivity $\rho_{\text{expt}} \approx 20\ \mu\Omega$ cm [10, 27]. Note that the area of the FS is always understood as being per spin except for the sum of the two spin channels ($\uparrow\downarrow$).

Orthorhombic		$\text{Tr}(n/m^*)_{\alpha\beta}$	$\langle v_{Fx}^2\rangle$	$\langle v_{Fy}^2\rangle$	$\langle v_{Fz}^2\rangle$	τ	ℓ	$\langle\rho\rangle$	S_{FS}
64 k-points in IBZ		(10^{51} kg^{-1} cm^{-3})	(10^{14} cm^2 s^{-2})			(10^{-14} s)	(Å)	($\mu\Omega$ cm)	(10^{17} cm^{-2})
Magnetic	($\uparrow$)	0.38	0.36	0.28	0.09	6.6	56	476	0.10
	($\downarrow$)	9.17	1.80	1.85	1.58	6.6	151	21	0.84
	($\uparrow\downarrow$)	9.55	1.45	1.48	1.23	6.6	135	20	0.95
Non-magnetic		10.25	0.64	0.69	0.78	6.1	89	20	0.78
Cubic		$\text{Tr}(n/m^*)_{\alpha\beta}$	$\langle v_{Fx}^2\rangle = \langle v_{Fy}^2\rangle = \langle v_{Fz}^2\rangle$			τ	ℓ	$\langle\rho\rangle$	S_{FS}
120 k-points in IBZ		(10^{51} kg^{-1} cm^{-3})	(10^{14} cm^2 s^{-2})			(10^{-14} s)	(Å)	($\mu\Omega$ cm)	(10^{17} cm^{-2})
Magnetic	($\uparrow$)	11.66	3.42			1.5	46	69	0.86
	($\downarrow$)	28.54	6.72			1.5	65	28	1.65
	($\uparrow\downarrow$)	40.20	5.25			1.5	58	20	2.51
Non-magnetic		48.72	1.80			1.3	29	20	2.31

Table 4. Transport properties for $CaRuO_3$ at $T = 0$. The DoS at ϵ_F can be obtained from table 2. The tensor $(n/m)_{\alpha\beta}$ is calculated from equation (2). The mean free path ℓ and the relaxation time τ have been calculated from the experimental resistivity $\rho_{\text{expt}} \approx 50\ \mu\Omega$ cm [10]. Note that the area of the FS is always understood as being per spin except for the sum of the two spin channels ($\uparrow\downarrow$).

Orthorhombic		$\text{Tr}(n/m^*)_{\alpha\beta}$	$\langle v_{Fx}^2\rangle$	$\langle v_{Fy}^2\rangle$	$\langle v_{Fz}^2\rangle$	τ	ℓ	$\langle\rho\rangle$	S_{FS}
216 k-points in IBZ		(10^{51} kg^{-1} cm^{-3})	(10^{14} cm^2 s^{-2})			(10^{-14} s)	(Å)	($\mu\Omega$ cm)	(10^{17} cm^{-2})
Magnetic	($\uparrow$)	1.02	0.59	0.66	1.35	3.6	58	299	0.15
	($\downarrow$)	5.43	0.63	0.92	0.54	3.6	52	60	0.69
	($\uparrow\downarrow$)	6.45	0.62	0.88	0.67	3.6	53	50	0.84
Non-magnetic		11.02	0.65	0.67	0.60	2.1	29	50	0.86
Cubic		$\text{Tr}(n/m^*)_{\alpha\beta}$	$\langle v_{Fx}^2\rangle = \langle v_{Fy}^2\rangle = \langle v_{Fz}^2\rangle$			τ	ℓ	$\langle\rho\rangle$	S_{FS}
120 k-points in IBZ		(10^{51} kg^{-1} cm^{-3})	(10^{14} cm^2 s^{-2})			(10^{-14} s)	(Å)	($\mu\Omega$ cm)	(10^{17} cm^{-2})
Non-magnetic		60.00	2.78			0.4	11	50	2.41

(which corresponds to an upwards shift of the minority-spin band of only 10 meV, and a change in the magnetic moment $\Delta\mu \approx +0.03\ \mu_B$/f.u.) shows that the 'lemon-like' sheet in figure 5(b) shrinks to a 'peanut-like' sheet around Γ. Shifting the majority-spin bands upwards by about 70 meV (corresponding to $\Delta\mu \approx -0.13\ \mu_B$/f.u.) shows that the sheet in figure 5(a) becomes almost degenerate with the 'lemon' of figure 5(b) and that a new sheet appears. Thus, since our calculated magnetic moment is not too far from the observed

values (see section 3.3) we expect that the FS of the most dispersive bands should be detectable. A comparison with de Haas–van Alphen data for these systems would provide a very precise check of the validity of the calculated band results.

3.2. Transport properties

In order to calculate the conductivity tensor $\sigma_{\alpha\beta}$ from the band structure, we have to estimate the relaxation time, τ. Among various possibilities [50], we chose the easiest one, i.e. τ independent of both ϵ and the DoS. At $T = 0$, one thus has $\sigma_{\alpha\beta} = e^2\tau(n/m^*)_{\alpha\beta}$, with $\alpha, \beta = x, y$ or z, where the $(n/m^*)_{\alpha\beta}$ tensor is [51]

$$\left(\frac{n}{m^*}\right)_{\alpha\beta} = \frac{1}{\Omega_{\text{cell}}} \sum_{n,\boldsymbol{k}\in\text{BZ}} v_{n\boldsymbol{k}\alpha} v_{n\boldsymbol{k}\beta} \delta(\epsilon_F - \epsilon_{n\boldsymbol{k}}). \tag{1}$$

Here the tensor $\sigma_{\alpha\beta}$ is diagonal and the average conductivity is $\langle\sigma\rangle = \frac{1}{3}\sum_\alpha \sigma_{\alpha\alpha}$. The velocities, $\boldsymbol{v}_{\boldsymbol{k}} = (1/\hbar)\partial\epsilon_{\boldsymbol{k}}/\partial\boldsymbol{k}$, were calculated using six auxiliary k-points for each k-point of the main mesh, and the sum in (1) was evaluated by the tetrahedron method [52–54]. Furthermore, one can define the average Fermi velocities

$$\langle v_{F\alpha}^2\rangle \equiv \frac{\Omega_{\text{cell}}}{N(\epsilon_F)}\left(\frac{n}{m^*}\right)_{\alpha\alpha} \tag{2}$$

that simplify the expression for the conductivity, which becomes $\sigma_{\alpha\alpha} = e^2 N(\epsilon_F)\langle v_{F\alpha}^2\rangle\tau$, where $N(\epsilon_F)$ is the DoS at ϵ_F.

To estimate the transport properties, we assumed that τ was the same for both channels. This is justified if there is a strong interaction between the electrons of different spins, or, in other words, if the scattering is dominated by the contribution of spins. An alternative approach is to consider the same mean free path for both spins, which amounts to considering almost entirely decoupled current channels in a scheme where the scattering is mainly due to impurities. In fact this second approach leads to very similar results, its main effect being to slightly decrease the anisotropy in the resistivity.

The transport properties of SRO and CRO are given in tables 3 and 4 respectively. The relaxation times were calculated from the experimental resistivities (at very low temperatures), and assuming that they are equal for the two spin channels, i.e. $\tau_\uparrow = \tau_\downarrow = \tau$. The measured resistivities at zero temperature are of about 20 $\mu\Omega$ cm for SRO [10, 27, 28] (a recent measurement showed half this value [23]) and 50 $\mu\Omega$ cm for CRO [10]. The mean free path is calculated simply as $\ell = \tau\sqrt{\sum_\alpha \langle v_{F\alpha}^2\rangle}$. In these tables, we also show the average resistivity $\langle\rho\rangle$ that we took from experiment, which is interesting for demonstrating the anisotropy between the two spin channels, and the area of the Fermi surface S_{FS}.

These results clearly show the large anisotropy in the resistivity of the two spin channels which appears to be more pronounced in the orthorhombic symmetry and particularly for the SRO where both $N(\epsilon_F)$ and the Fermi velocities $\langle v_F^2\rangle$ play a role. This shows that these materials are very close to being in a semi-metallic state. The relaxation times for the orthorhombic cases seem comparable to the Drude results [55]. That the relaxation times τ for the cubic systems are much smaller (5–10 times) can be understood because these systems are expected to be better conductors (so fitting τ to the experimental value underestimates it). For cubic compounds, $N(\epsilon_F)\langle v_F^2\rangle$ is indeed 5–10 times larger (tables 3 and 4). Furthermore, one expects τ_{ortho} to be smaller than τ_{cubic}, since the distortion adds variations to the cubic potential that tend to increase the scattering rate. Thus if cubic systems could be stabilized, they would have a much larger conductivity (at least 5–10 times).

The anisotropy of the mean free paths $\ell_\uparrow$ and $\ell_\downarrow$ reflects the anisotropy of the average Fermi velocity. For SRO, it is very large, whereas for CRO, it is almost negligible and there the anisotropy in the resistivity is entirely due to the difference in the DoS. These results scale with the resistivity in the first approximation. Therefore at room temperature, τ and ℓ should decrease by a factor of about 10 for SRO and of about 5 for CRO [10, 27, 28], and thereby be at the limit of the Boltzmann theory [51].

A knowledge of the area of the FS permits an independent estimation of the mean free path ℓ through the equation [33, 51]

$$\sigma = \frac{e^2}{24\pi^3\hbar}(S_{FS\uparrow}\ell_\uparrow + S_{FS\downarrow}\ell_\downarrow) \tag{3}$$

which gives a robust result as long as ℓ_k does not vary too much over the FS. The mean free paths estimated in this way tend to be slightly larger than those calculated from τ. For spin-polarized SRO, we obtained $\ell = 60$ and 155 Å in the cubic and orthorhombic structures respectively, and for CRO, 13 and 71 Å.

3.3. Magnetic properties

Non-spin-polarized calculations are used to determine the Stoner enhancement factor,

$$S = \frac{1}{(1 - \bar{S})} \tag{4}$$

to find the criterion for a magnetic instability of these systems, i.e. when $\bar{S} = 1$. This Stoner enhancement factor, S, also gives the susceptibility enhancement as the ratio between the internal and an applied magnetic field [56–58]. The spin-polarized calculation directly gives the magnetic moment, μ, i.e. the difference between the total numbers of spin-up and spin-down electrons which corresponds to the 'saturated magnetic moment', μ_{sat}, at $T = 0$. The differences in total energy between the two calculations are used to determine the stability of the magnetic state.

The results are presented in table 5. They all show magnetic moments, except the cubic CRO. We want to emphasize here that calculations with other parameters (linearization energies, etc) can give magnetic solutions for cubic CRO as well. This shows the sensitivity of these systems. But the results that we show in the figures and tables are for parameters as close as possible in all of the structures, magnetic or non-magnetic cases, for SRO and CRO. For the orthorhombic structure, SRO and CRO have almost the same μ. That the Stoner factor, $\bar{S}$, for SRO is less than one is rather puzzling, but can be explained by the position of the Fermi level on a very steep slope of a subpeak in the DoS, and a very small shift in ϵ_F can change $\bar{S}$ to more than one (for example, a shift of -6 mRyd implies an $\bar{S}$ of 1.06). In the case of cubic CRO, the Stoner factor also disagrees with the result of the magnetic calculation. This can also be explained by the position of ϵ_F on the slope of one of the secondary peaks, but, as we have just mentioned above, the magnetic properties of CRO are extremely sensitive to the calculation parameters.

The magnetic solutions are always lower in energy than the corresponding non-magnetic ones. For SRO, the gain is 1.67 eV/f.u. for both cubic and orthorhombic symmetries, and for orthorhombic CRO, it is 1.40 eV/f.u.. This is approximately three times larger than the result of Singh [46].

The magnetic moments μ are dominated by the contribution of the Ru due to its high DoS, and there is a weak polarization on O sites mainly through hybridization with the Ru d band. The total magnetic moments are larger than the experimental results for μ_{sat} which are between 0.8 and 1.6 μ_B [25, 27, 28]. This discrepancy may be due to finite-temperature

effects lowering the magnetization, or, as pointed out by Kanbayashi, to the multidomain structure [30] and the magnetocrystalline anisotropy [26]. An alternative explanation is that our calculation overestimated the hybridization somehow, thus amplifying the contribution of the O. Using a simple spin-only magnetism approach, the 'effective magnetic moment', $\mu_{\rm eff}$, can be estimated as $\mu_{\rm eff} = \sqrt{\mu(\mu + g_0)}$ (where g_0 can be taken as 2). We obtain that $\mu_{\rm eff} = 2.8\ \mu_B$ for both orthorhombic SRO and CRO calculations, and $\mu_{\rm eff} = 2.5\ \mu_B$ for cubic SRO. The experimental results for $\mu_{\rm eff}$ vary from 2–2.6 μ_B (with the variation ascribed to differences in sample quality) [25, 27, 28], and our values lie close to this range.

Our present results for the magnetic moment μ are larger than both those of our previous calculation [33] and those of Singh [46]. This is an indication that although the trend is certainly correct, the detailed calculated results may not always be very accurate. However, we think that this is connected with some real properties of these materials and is consistent with the relatively wide spread of many of the experimental results.

Table 5. Magnetic properties of SRO and CRO for the cubic and the real orthorhombic structures. We show the contribution of each atom to the magnetic moment in μ_B/f.u., and the Stoner factor $\bar{S}$ (from the non-spin-polarized cases).

	$SrRuO_3$					$CaRuO_3$				
	Magnetic moment μ (μ_B/f.u.)				Stoner	Magnetic moment μ (μ_B/f.u.)				Stoner
	Sr	Ru	O_3	Total	$\bar{S}$	Ca	Ru	O_3	Total	$\bar{S}$
Orthorhombic	0.08	1.58	0.30	1.96	0.93	0.06	1.61	0.26	1.93	1.18
Cubic	0.06	1.41	0.26	1.73	1.89	0	0	0	0	1.06

4. Discussion

4.1. Comparison with spectroscopic data and other calculations

We have compared the calculated DoS with the photoemission and EELS spectra obtained by Cox *et al* [59]. Although this comparison is only qualitative, the agreement is quite good for both SRO and CRO (whose spectra are very similar). Indeed, apart from a small shift which can probably be ascribed to some spectral weight redistribution as in Sr_2RuO_4 [60], the positions of the peaks in the DoS agree quite well with the UV photoelectron spectroscopy (UPS) data. However, the Ru d peak at ϵ_F is much suppressed in the experimental spectra. This can be due either to some peculiar 'joint DoS' property, i.e. that the DoS near $\epsilon_F + \bar{h}\omega$ is very small, or that the matrix elements for the d $\rightarrow$ f and d $\rightarrow$ p transitions are small (a preliminary calculation seems to support the latter). A similar situation occurs in $BaRuO_3$ where the contribution of the Ru d DoS at ϵ_F is also much suppressed in the UPS results (for both $h\nu = 21.2$ and 40.8 eV) whereas it appears clearly in XPS [5]. The bump in the EELS spectra (at about 3 eV above ϵ_F) seems to be linked with the Sr d or Ca d features in the DoS above ϵ_F. However, this is in contradiction with the assignment of the EELS feature to the $t_{2g} \rightarrow e_g$ transition by Cox *et al* [59]. We have also compared the calculated core levels with the core-level photoelectron spectrum for SRO [59]. Again, there is a good qualitative agreement. As expected, since we have not used the 'final-state rule' [61], the absolute positions are higher than the measured ones (by about 20 eV).

Comparing our bands (figure 1) with those of Singh [46], it appears that the main

difference is that the Ru d block is shifted downwards in Singh's calculation relative to ours. This has the effect of closing the gap below ϵ_F and moving the Sr d and Sr s states away from ϵ_F. Otherwise, the agreement is rather close. The DoS at ϵ_F for the orthorhombic SRO is smaller than in both our previous and Singh's calculation, resulting in a much larger enhancement factor of $1 + \lambda = \gamma_{\rm exp}/\gamma_{\rm th} \approx 6.2$ [33] than for the case of Sr_2RuO_4 [63, 64]. This strongly depends on the exact position of ϵ_F, as was the case for the transport properties, which depend on $N(\epsilon_F)$ and $\langle v_F^2 \rangle$. Again, we conclude that the special sensitivity of ϵ_F, relative to the DoS peak in these systems, leads us to rely on the main trends rather than details. But the difference between the unenhanced theoretical DoS and the experimental specific heat is very large. A large electron–phonon coupling seems possible because of the large DoS, but also large enhancements due to spin fluctuations are likely in systems which are close to a magnetic transition.

4.2. Sensitivity of the calculated solutions

As we have already mentioned, these materials are very sensitive to changes in calculation parameters. This is due to the very large and almost isolated peak at ϵ_F, since a very small change in ϵ_F can have quite a large effect on the transport properties that depend on the DoS at ϵ_F or on the spin splitting, and this is more important since it has some influence on the convergence.

In order to estimate the amplitude of these effects, we have performed the calculations for many different situations. First, we checked that the slight difference between the experimental structural data from Shikano *et al* [20] and Kobayashi *et al* [19] (orthorhombic symmetry) has only minor effects on the band results. We also tested the effect of the 'muffin-tin' radius $r_{\rm MT}$ on the results. An increase in $r_{\rm MT}$ for Ru by 2% (and a corresponding scaling down of the others) for the cubic case will slightly reduce the gap below ϵ_F and thus slightly decrease the magnetic moment. Changing the linearization energy, ϵ_ν, can be more crucial. Indeed, due to the large bandwidth to be linearized, the results are very sensitive to the setting of ϵ_ν. As was mentioned earlier for cubic CRO, a modification of the parameters can change the calculated magnetic properties drastically. We have made two other spin-polarized calculations which differ from the first one by the fact that Ca 3p electrons are not included in the valence and from each other by different choices for $r_{\rm MT}$. The magnetic moments, μ, were about 1.6 μ_B in both cases, and the Stoner factors, $\bar{S}$, for the corresponding non-spin-polarized calculations were about 1.1 (slightly larger than the result shown in table 5). The reason for this sensitivity is probably linked to the value of ϵ_ν. Nevertheless, the choice of ϵ_ν in the first calculation seems justified since this calculation is the closest to the SRO cubic calculation and therefore the best for isolating the effect of the substitution of Ca for Sr. Furthermore, even the magnetic solutions for CRO show roughly the same tendency as the experiment, i.e. a decreasing magnetic moment with increasing pressure [20, 31]. This trend is confirmed by a cubic calculation for SRO with a compressed cell (9%) showing a reduction of μ of about 0.09 μ_B Å^{-3}. This sensitivity can partly be understood in view of the surprisingly large observed influence of the Na doping on SRO and CRO which was interpreted in terms of volume reduction [40]. But an alternative explanation is that the charge is decreasing because Na has one fewer valence electron than Sr, so from rigid-band arguments ϵ_F should also drop to lower energies where the DoS is smaller, and the Stoner factor is expected to decrease. A further experimental illustration of the variation of the properties in these materials is the 60° twin observed in SRO that is undetectable by normal test procedures [62] and it could explain the smaller magnetic moments found in the experiments.

4.3. Magnetic properties

The difference between the calculated magnetic properties of cubic SRO and CRO can be understood in view of the subtle but important difference between the two electronic structures (see figures 1 and 2). In SRO, the high peak near ϵ_F originates from extended flat portions of the bands, such as, for instance, the flat bands just below ϵ_F on the path Γ–X–M. In CRO, the corresponding bands show a larger dispersion due to accidental degeneracies at M and band crossings with other bands between Γ and X. This results in a two-peak structure with ϵ_F lying in between. Thus, the DoS at ϵ_F, $N(\epsilon_F)$, and consequently the Stoner factor $\bar{S}$ are lower for CRO (see tables 1, 2 and 5) and are apparently not sufficient for a Stoner splitting.

When the orthorhombic distortion occurs, many degeneracies are lifted due to the lower symmetry. Therefore, the few-peak DoS structure for the cubic systems is replaced by a multi-peak structure, as can be seen in figure 3. If, as in cubic SRO, ϵ_F is at exactly the position of the peak, the splitting of this peak by the distortion is likely to reduce $N(\epsilon_F)$ and $\bar{S}$, whereas they are likely to increase if ϵ_F is between two peaks, as is the case for cubic CRO. This can explain the different behaviours of $\bar{S}$ when the distortion is introduced, i.e. that it diminishes in the case of SRO and increases for CRO (see table 5). Furthermore, the apparent inconsistency between the spin-polarized calculation and the Stoner factor for orthorhombic SRO can partly be explained since $\bar{S}$ is lowered if there is a strong hybridization between spin-split bands and bands resisting spin splitting [56], which may be the case here. This shows that a case with a large Stoner factor does not necessarily imply a large moment. A magnetic transition is predicted because $\bar{S} \geqslant 1$, but the size of the moment depends also on the width of the DoS peak.

For orthorhombic SRO, the calculated results agree rather well with experiment, while this is not the case for CRO. It is clear that for the many-peak DoS function shown in figure 3, the condition for having a magnetic ordering is extremely sensitive to the very precise position of the Fermi level. A single-iteration calculation with 1331 k-points in the IBZ for orthorhombic SRO shows that this multi-peak structure is essentially stable with respect to the number of k-points used, so only other details of the computational scheme (type of density functional potential, non-spherical corrections, spin–orbit coupling, etc) could have a sufficient influence on the DoS to make CRO non-magnetic. From our calculations, it seems that, within the LSDA, the orthorhombic distortion favours spin-split states. Thus the fact that we obtain a ferromagnetic ground state instead of a non-magnetic one in orthorhombic CRO could be interpreted as the signature of an underlying antiferromagnetic ground state [65]. Indeed, since the magnetic moments are essentially localized at (presumably weakly coupled) Ru sites, with only small moments in between (mainly at O sites), both ferromagnetic and antiferromagnetic ordering should be favoured. Whether this is the case has to be checked by a calculation with an antiferromagnetic configuration.

Although it is clear that the magnetism in these systems is due to the Ru d electrons, there have been various arguments about the importance of e_g and t_{2g} symmetry within the d band. Our calculations for the cubic case show that both e_g and t_{2g} electrons are important for the magnetism in contradiction with the hypothesis of Callaghan *et al* [24]. This is particularly striking with the disappearance (or at least diminution) of the magnetism with the splitting of the e_g and t_{2g} peaks in the DoS near ϵ_F upon doping with Ca (figure 2). In the real structure, the Ru d bands show strong mixing of e_g or t_{2g} symmetries, and it is difficult to discuss the effect of the splitting of the t_{2g} bands on ferromagnetism or antiferromagnetism as Fukunaga and Tsuda [39] did. But it is clear that the distortion lifts the degeneracy (in

conflict with the observation of Gibb *et al*, that the distortion has a negligible effect on the t_{2g} bands [36]). Moreover, our calculations are in contradiction with the idea of Kanbayashi about the role of the orthorhombic distortion as regards the magnetism [38] (i.e. that this distortion destroys the magnetism) since the calculated moments are larger for the real structure. A similar kind of sensitivity of the magnetic properties to the structure has recently been found in another perovskite-like compound: $LaMnO_3$ [66]. There, the cubic structure exhibits ferromagnetism whereas the real orthorhombic one shows antiferromagnetism. This confirms that the properties of these systems can exhibit large variations for small external changes.

Nevertheless, we believe that our calculated electronic and magnetic properties are close to reality and that the unusual sensitivity of the magnetic ordering (that shows up as a 'wrong' result for CRO) reveals a real sensitivity of the magnetism in these systems. A small perturbation, such as a departure from stoichiometry, structural distortions, and charge transfers near interfaces or surfaces, can be sufficient to cause both SRO and CRO to show magnetism or not.

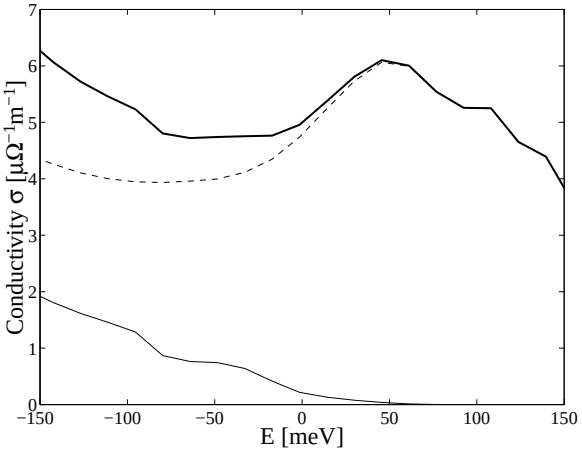

Figure 6. The conductivity of SRO (orthorhombic symmetry) in $\mu\Omega^{-1}$ m^{-1} as a function of the energy ($\epsilon_F = 0$ here). The majority-spin contribution (light, plain line), the minority-spin (dashed line), and the total (heavy line) contributions are represented. The experimental conductivity is 5 $\mu\Omega^{-1}$ m^{-1} (see table 3). The energy dependence of the conductivity is obtained through a simple rigid-band approximation. The relationship between the shift in energy and the surface polarization charge is almost linear in this region and, for the case of a layer 10 Å thick, a polarization charge of 50 μC cm^{-2} corresponds to a shift in energy of 87 meV.

4.4. Effects in SRO thin films

Since in most of the applications these compounds are used as thin films grown on a $SrTiO_3$ substrate, we have investigated the effect of the lattice mismatch for the case of cubic SRO in order observe the general trend (neglecting the effect of the interface). We have examined two cases: the reduction of the *a* and *b* lattice parameters by 2% and 3%, while the *c* lattice parameter is increased in order to conserve the volume. The effect of these distortions on the DoS is mainly that of splitting the peak at ϵ_F in a somewhat similar manner to that for the Ca substitution (although, here, it is due to the non-equivalence of X and Z and the flat bands near X lie lower near Z). The magnetic moment, μ, is thereby

reduced to 1.59 μ_B for 2% and to 1.44 μ_B for 3% distortion. This trend for μ provides an alternative explanation of the smaller magnetic moment observed in thin films. Finally, another interesting technical application of SRO thin films is the growth of ferroelectric heterostructures with PZT [15–17, 23, 67]. The fact that SRO is so close to being in a semi-metallic state could be exploited, especially in ultrathin films, by polarizing the PZT. Indeed, the effect of the surface charge induced by the polarization is, in the rigid-band approximation, to shift ϵ_F. Within a very simple model where these charges are considered as homogeneous in a layer of thickness d, the relation between the shift in energy $\Delta\epsilon$ and the surface charge σ is simply $\sigma = (n(\epsilon_F+\Delta\epsilon)-n(\epsilon_F))q_e d/\Omega_{\text{cell}}$ where $n(\epsilon)$ is the number of (valence) electrons up to energy ϵ and q_e the electronic charge. The dependence of the conductivity on the shift in energy for the orthorhombic case is shown in figure 6. From the aforementioned arguments, a surface charge of 50 μC cm^{-2} corresponds to a shift of ϵ_F of 87 meV for a layer 10 Å thick. In such a situation, an ≈8% change of the conductivity can be achieved by flipping the polarization. However, this is only approximate since the conductivity has local extrema in the region of interest, being therefore very sensitive to the shift in energy [68]. For instance, the same charge with a layer 30 Å thick gives an ≈20% change. A surface charge of about 50 μC cm^{-2} is needed to transform an SRO layer 10 Å thick into a semi-metal. For such a charge, the magnetic moment is decreased by about 7%, this decrease scaling almost linearly with the charge (in the cubic case, the decrease is only about 2%). Although such polarization charges can be achieved with PZT (a 10% change has been demonstrated in ultrathin (30 Å) SRO films using polarization fields of about 10–15 μC cm^{-2} [16, 17, 23]), the semi-metallic effects would be washed out by the averaging over the actual film's thickness. Nevertheless, one could still hope to achieve an observable effect on the magnetic moment (at low temperature). Since the majority DoS is decreasing and the minority is increasing at ϵ_F, an applied magnetic field could also have a similar effect on SRO. Therefore a calculation with a field of about 40 T (which becomes Stoner enhanced by a factor of about 3) has been carried out. The induced changes in the properties are very small: the DoS at ϵ_F is decreased by about 3%, the resistivity by about 1%, and the spin splitting is increased by 6 meV (≈1%). The majority-spin semi-gap which lies 96 meV away from ϵ_F comes closer to ϵ_F by 2 meV. Thus important changes in the properties at $T = 0$ would require unfeasibly large magnetic fields, at least in this case.

5. Conclusion

We have studied the properties of SRO and CRO in cubic and real orthorhombic structures by means of self-consistent LMTO band calculations. The question of structural phase stability is not investigated here because of the spherical potential approximation, but many other properties are not affected by this approximation. The LMTO results for SRO and CRO show an unusual sensitivity to calculational details. This sensitivity is mainly due to the fact that ϵ_F falls near a sharp increase of the DoS. The position of ϵ_F thus has a great impact on the physical properties, since most of them depend precisely on the Fermi surface shape as well as on the DoS at ϵ_F. For instance, the criterion for a ferromagnetic transition depends critically on the DoS value at ϵ_F, and therefore only a small change is needed to make the difference between a non-magnetic and a spin-polarized solution. Our calculations show that the SRO is ferromagnetic with a magnetic moment of 1.96 μ_B/f.u. (1.73 in the simple cubic symmetry). Although this moment is larger than the experimental value (this can partly be explained by temperature effects), it is a manifestation of the unusual sensitivity to the position of ϵ_F. Nevertheless our results show that this compound is a good example of band ferromagnetism. The tendency towards magnetism in CRO is weaker. In the

simple cubic structure, the corresponding calculation even gives a paramagnetic solution, whereas the real orthorhombic structure is ferromagnetic, with a moment of 1.93 μ_B/f.u.. The possibility of an antiferromagnetic character of CRO needs to be confirmed by a proper calculation for an antiferromagnetic configuration.

The calculation in the cubic case shows the importance of both the Ru d e_g and t_{2g} bands for the high peak in the DoS that is responsible for the magnetism. However, in the calculations for the real structure, the d bands have no clearly defined e_g or t_{2g} symmetries, but have a mixture of these, even in the case of the relatively small distortion of SRO. It is therefore impossible to isolate a Ru d sub-band that would be the only one responsible for the magnetism in this compound.

If the magnetic moment is sensitive, it also follows that the transport properties, which are determined by the majority and minority FS properties, are sensitive. For instance, Fermi velocities and FS topologies are completely different for magnetic and non-magnetic solutions.

The calculated transport properties clearly show the importance of the orthorhombic distortion as regards explaining the observed poor metallic behaviour of these oxides [27, 28]. Indeed, the cubic structure would lead to good conductivity. Moreover this distortion is crucial for the opening of the semi-gap just above ϵ_F. This gap structure for the majority-spin electrons is so close to ϵ_F that the semi-metallic state can possibly be entered by ultrathin films on a polarized ferroelectric (by charge transfers). Another interesting feature of the physical properties of these materials is that ϵ_F lies on a very steep slope of the DoS. This condition is important to a tiny change of ϵ_F (due either to charge transfers, or to shear, or to a magnetic field) being able to induce an observable change in the resistivity [16, 17].

Finally, our calculations show that the large variety of interesting physical properties that have been observed for these compounds can be understood as an effect of the position of ϵ_F on the steep edge of a large peak in the DoS.

Acknowledgments

We want to thank here P B Allen for having aroused our interest in these systems and for stimulating discussions, and C H Ahn, L Miéville, J-M Triscone, L Antognazza, B Revaz and F Bonhomme for interesting and helpful discussions. We are also grateful to S Dugdale for his careful reading of this manuscript. This work was supported in part by the Swiss National Science Foundation.

References

[1] Randall J J and Ward R 1959 *J. Am. Chem. Soc.* **81** 2629
[2] Maeno Y, Hashimoto H, Yoshida K, Nishizaki S, Fujita T, Bednorz J G and Lichtenberg F 1994 *Nature* **372** 532
[3] Maeno Y and Yoshida K 1996 *Proc. 21st Conf. on Low Temperature Physics; Czech. J. Phys. Suppl.* S6 **46** 3097
[4] Cava R J, Zandbergen H W, Krajewski J J, Peck W F Jr, Batlogg B, Carter S, Fleming R M, Zhou O and Rupp L W Jr 1995 *J. Solid State Chem.* **116** 141
[5] Gulino A, Egdell R G, Battle P D and Kim S H 1995 *Phys. Rev.* B **51** 6827
[6] Scott J F and Paz de Araujo C A 1989 *Science* **246** 1400
[7] Prins M W J, Grosse-Holz K-O, Müller G, Cillessen J F M, Giesbers J B, Weening R P and Wolf R M 1996 *Appl. Phys. Lett.* **68** 3650
[8] Eom C B, Cava R J, Fleming R M, Phillips J M, van Dover R B, Marshall J H, Hsu J W P, Krajewski J J and Peck W F Jr 1992 *Science* **258** 1766

[9] Miéville L, McGuirk J, Geballe T H, Antognazza L and Char K 1996 *Proc. 21st Conf. on Low Temperature Physics; Czech. J. Phys.* **46** 2105
Miéville L, Geballe T H, Antognazza L and Char K 1997 *Appl. Phys. Lett.* **70** 126
Miéville L 1995 *PhD Thesis* University of Geneva
[10] Bouchard R J and Gillson J L 1972 *Mater. Res. Bull.* **7** 873
[11] Wu X D, Foltyn S R, Dye R C, Coulter Y and Muenchausen R E 1993 *Appl. Phys. Lett.* **62** 2434
[12] Antognazza L, Char K, Geballe T H, King L L H and Sleight A W 1993 *Appl. Phys. Lett.* **63** 1005
[13] Gausepohl S C, Lee M, Antognazza L and Char K 1995 *Appl. Phys. Lett.* **67** 1313
[14] Miéville L, Koller E, Triscone J-M, Decroux M, Fischer Ø and Williams E J 1996 *Phys. Rev.* B **54** 9525
Miéville L, Koller E, Triscone J-M and Fischer Ø 1994 *Physica* C **235–240** 725
[15] Eom C B, Van Dover R B, Phillips J M, Werder D J, Marshall J H, Chen C H, Cava R J, Fleming R M and Fork D K 1993 *Appl. Phys. Lett.* **63** 2570
[16] Ahn C H, Hammond R H, Geballe T H, Beasley M R, Triscone J-M, Decroux M, Fischer Ø, Antognazza L and Char K 1997 *Appl. Phys. Lett.* **70** 206
[17] Ahn C H, Antognazza L, Tybell T, Char K, Decroux M, Hammond R H, Geballe T H, Beasley M R, Fischer Ø and Triscone J-M 1996 *J. Low Temp. Phys.* **105** 1517
[18] Jones C W, Battle P D, Lightfoot P and Harrison W T A 1989 *Acta Crystallogr.* C **45** 365
[19] Kobayashi H, Nagata M, Kanno R and Kawamoto Y 1994 *Mater. Res. Bull.* **29** 1271
[20] Shikano M, Huang T-K, Inaguma Y, Itoh M and Nakamura T 1994 *Solid State Commun.* **90** 115
[21] Catchen G L, Rearick T M and Schlom D G 1994 *Phys. Rev.* B **49** 318
[22] Cuffini S L, Guevara J A and Mascarenhas Y P 1996 *Mater. Sci. Forum* **228** 789
[23] Ahn C H and Triscone J-M 1997 *Preprint*
Ahn C H and Triscone J-M 1997 Private communication
[24] Callaghan A, Moeller C W and Ward R 1966 *Inorg. Chem.* **5** 1572
[25] Longo J M, Raccah P M and Goodenough J B 1968 *J. Appl. Phys.* **39** 1327
[26] Kanbayashi A 1976 *J. Phys. Soc. Japan* **41** 1876
Kanbayashi A 1976 *J. Phys. Soc. Japan* **41** 1879
[27] Klein L, Dodge J S, Ahn C H, Snyder G J, Geballe T H, Beasley M R and Kapitulnik A 1996 *Phys. Rev. Lett.* **77** 2774
[28] Klein L, Dodge J S, Ahn C H, Reiner J W, Miéville L, Geballe T H, Beasley M R and Kapitulnik A 1996 *J. Phys.: Condens. Matter* **8** 10 111
[29] Klein L, Dodge J S, Geballe T H, Kapitulnik A, Marshall A F, Antognazza L and Char K 1995 *Appl. Phys. Lett.* **66** 2427
[30] Kanbayashi A 1978 *J. Phys. Soc. Japan* **44** 89
[31] Neumeier J J, Cornelius A L and Schilling J S 1994 *Physica* B **198** 324
[32] Kiyama T, Yoshimura K, Kosuge K, Ikeda Y and Bando Y 1996 *Phys. Rev.* B **54** R756
[33] Allen P B, Berger H, Chauvet O, Forro L, Jarlborg T, Junod A, Revaz B and Santi G 1996 *Phys. Rev.* B **53** 4393
[34] Gausepohl S C, Lee M, Rao R A and Eom C B 1996 *Phys. Rev.* B **54** 8996
[35] Gausepohl S C, Lee M, Char K, Rao R A and Eom C B 1995 *Phys. Rev.* B **52** 3459
[36] Gibb T C, Greatrex R, Greenwood N N and Kaspi P 1973 *J. Chem. Soc. Dalton Trans.* 1253
[37] Gibb T C, Greatrex R, Greenwood N N, Puxley D C and Snowdon K G 1974 *J. Solid State Chem.* **11** 17
[38] Kanbayashi A 1978 *J. Phys. Soc. Japan* **44** 108
[39] Fukunaga F and Tsuda N 1994 *J. Phys. Soc. Japan* **63** 3798
[40] Shepard M, Cao G, McCall S, Freibert F and Crow J E 1996 *J. Appl. Phys.* **79** 4821
[41] Noro Y and Miyahara S 1969 *J. Phys. Soc. Japan* **27** 518
[42] Kirillov D, Suzuki Y, Antognazza L, Char K, Bozovic I and Geballe T H 1995 *Phys. Rev.* B **51** 12 825
[43] Castelpoggi F, Morelli L, Salva H R, Cuffini S L, Carbonio R and Sanchez R D 1997 *Solid State Commun.* **101** 597
[44] Snyder G J, Moler K A, Beasley M R and Geballe T H 1996 *Preprint*
[45] Takegahara K 1994 *J. Electron Spectrosc. Relat. Phenom.* **66** 303
[46] Singh D J 1996 *J. Appl. Phys.* **79** 4818
[47] Andersen O K 1975 *Phys. Rev.* B **12** 3060
[48] Jarlborg T and Arbman G 1977 *J. Phys. F: Met. Phys.* **7** 1635
[49] Kohn W and Sham L J 1965 *Phys. Rev.* **140** A1133
[50] Allen P B, Pickett W E and Krakauer H 1988 *Phys. Rev.* B **37** 7482
Allen P B, Pickett W E and Krakauer H 1987 *Phys. Rev.* B **36** 3926
[51] Allen P B 1996 *Quantum Theory of Real Materials* ed J R Chelikowsky and S G Louie (Boston, MA: Kluwer)

ch 17, pp 219–50
[52] Lehmann G and Taut M 1972 *Phys. Status Solidi* b **54** 469
Lehmann G, Rennert P, Taut M and Wonn H 1970 *Phys. Status Solidi* **37** K27
[53] Jepsen O and Anderson O K 1971 *Solid State Commun.* **9** 1763
[54] Rath J and Freeman A J 1975 *Phys. Rev.* B **11** 2109
[55] Ashcroft N W and Mermin N D 1976 *Solid State Physics* (New York: Holt-Saunders)
[56] Jarlborg T and Freeman A J 1980 *Phys. Rev.* B **21** 2332
[57] Gunnarson O and Lundquist B I 1976 *Phys. Rev.* B **13** 4274
[58] Gunnarson O 1976 *J. Phys. F: Met. Phys.* **6** 587
[59] Cox P A, Egdell R G, Goodenough J B, Hammett A and Naish C C 1983 *J. Phys. C: Solid State Phys.* **16** 6221
[60] Inoue I H, Makino H, Aiura Y, Hase I, Maeno Y, Haruyama Y, Nishizaki S, Fujita T and Nishihara Y 1996 *Proc. 21st Conf. on Low Temperature Physics; Czech. J. Phys. Suppl.* S5 **46** 2699
[61] Lerch P, Jarlborg T, Codazzi V, Loupias G and Flank A M 1992 *Phys. Rev.* B **45** 11 481
[62] Fahey K P, Clemens B M and Wills L A 1995 *Appl. Phys. Lett.* **67** 2480
[63] Oguchi T 1995 *Phys. Rev.* B **51** 1385
[64] Singh D J 1995 *Phys. Rev.* B **52** 1358
[65] The configuration for our calculations can only give ferromagnetic or non-magnetic results. Thus, if the ground state is a 'spin-split' state (i.e. either a ferromagnetic, ferrimagnetic, or antiferromagnetic state), the LSDA solution would presumably be ferromagnetic instead of non-magnetic.
[66] Pickett W E and Singh D J 1996 *Phys. Rev.* B **53** 1146
[67] Ahn C H, Triscone J-M, Archibald N, Decroux M, Hammond R H, Geballe T H, Fischer Ø and Beasley M R 1995 *Science* **269** 373
[68] The shift in energy itself is not very accurate since it depends strongly on the 'effective' thickness of the layer (i.e. except perhaps for extremely thin layers, the charge is certainly not homogeneous and some averaging has to be done) and on the properties at ϵ_F.